Equation-of-State Measurements in Ta_2O_5 Aerogel

Introduction

In the last 15 years, there has been considerable interest in experiments that use laser-driven shock waves to measure high-energy-density equation-of-state (HED-EOS) data.[1–5] During this time, the generation of laser-driven shock waves has been refined, and the accuracy of the techniques employed has been improved significantly. Highly accurate optical studies of SiO_2 with laser-driven shock waves have shown strong agreement with experimental results obtained with other established drivers;[6] these measurements have extended the available data to many millions of atmospheres and identified new mechanisms that affect the material's HED-EOS.[7] Many HED-EOS experiments use standards or reference materials to which the behavior of the studied material is compared. These impedance-matching experiments are particularly important in laser-driven shock-wave experiments where nonreferenced HED-EOS measurements are complex.[8,9] The measurements on SiO_2 and the consistent structure of quartz lend themselves to the establishment of quartz as a standard material, as will be demonstrated in this study.

While shock waves in a material in its standard state can produce a wide range of pressures (depending upon the strength of the shock wave), the density and temperature states attainable are limited to the locus of solutions for the hydrodynamic equations commonly known as the principal Hugoniot of the material. One method to expand the attainable states from shock waves is to alter the initial density of the study material.[10] Experiments on these porous materials then enable the researcher to attain measurements of the material's HED-EOS over a broad range of conditions. Additionally, experiments on porous materials have also been used to understand the exotic shock phenomenon of supersonic, radiative transport.[11]

In supersonic radiative transport, the radiative flux from a shock front exceeds the material flux, indicating that the radiation front advances faster than the material shock front.[12] The experimental study in Ref. 11 used tantalum pentoxide (Ta_2O_5) aerogels as a host material for the study of radiative transport. These low-density aerogels were shocked to pressures over a million atmospheres, and both the radiation and hydrodynamics were tracked experimentally. However, to fully understand this experiment and future experiments with this material, reliable radiation-hydrodynamic (RadHydro) simulations are needed, which requires an understanding of the HED-EOS of the study material. To date, there were no HED-EOS measurements to provide guidance for the development of theoretical models of this high-porosity material.

This study provides accurate EOS measurements on Ta_2O_5 aerogel material to support model development. It uses the accumulated developments in laser-driven shock waves and their diagnosis to obtain compression and temperature data at pressures up to 3 Mbar (~3×10^6 atm). At these pressures, the Ta_2O_5 aerogels compress over four times their initial density and achieve temperatures $\geq$5 eV ($\geq$60,000 K). The aerogel densities used in this study are 0.1, 0.15, and 0.25 g/cm^3, far smaller than the solid-state density of this material, 8.2 g/cm^3. Twelve beamlines of the OMEGA Laser System[13] generated experimental pressures up to 1.25 Mbar in the 0.1-g/cm^3 aerogel and up to 3 Mbar in the 0.25-g/cm^3 aerogel. Since the material is transparent, the shock velocity was diagnosed with Doppler interferometry,[14] and the temperature was diagnosed with a streaked optical pyrometer.[15] Impedance-matching experiments were performed using two reference standards: aluminum (a legacy standard) and alpha quartz.

The shock-wave driver, diagnostics, and experimental materials necessary for this study will be discussed in the next section. The remaining sections (1) give important experimental observations, including the physical properties of the Ta_2O_5 aerogel samples (refractive index and density as well as the manufacturing residuals present), the measurements that justify the use of quartz as a reference material, and the EOS measurements (density, temperature, and pressure) of the HED Ta_2O_5; (2) discuss the EOS measurements with respect to the available qEOS model; (3) address a diagnostic modification that could benefit future studies of this type; and (4) present conclusions.

Experimental Technique

This experimental study used laser-driven shock waves to achieve the desired states required for HED-EOS model refinement. The OMEGA laser[13] is the driver for the experiments; the diagnostics were the velocity interferometer system for any reflector (VISAR)[14] and the streaked optical pyrometer (SOP).[15] Using these two diagnostics, it is possible to completely determine the EOS of a material using the impedance-matching technique. These diagnostics operate on a subnanosecond time scale so that they can fully capture the material response over the entire multinanosecond OMEGA laser pulse. The millimeter-scale targets of this study were precision manufactured, machined, and assembled through a collaboration between technicians in the LLE Target Fabrication Group and chemists at the Lawrence Livermore National Laboratory Target Fabrication Group.

OMEGA is a 60-beam, 351-nm, third-harmonic Nd:glass laser system designed for spherical illumination of imploding spherical targets.[13] To produce shocks in these planar EOS targets, up to 12 of the OMEGA beamlines irradiate the target package. Six of these beams have an angle of incidence of 23° with respect to the target normal; the other six are incident at 48°. All of the beams are focused (at *f*/6.7) to the same spot on the target. Each beam was outfitted with a distributed phase plate[16] that produces a super-Gaussian intensity distribution at the target with a full width at half maximum (FWHM) of approximately 800 μm. A 3.7-ns, flattop pulse shape was used to maximize the steadiness of the shock-wave front while minimizing the coronal temperature for the desired experimental conditions. The total energy per beamline was ~240 J of 351-nm radiation, yielding irradiances in the range of 15 to 80 TW/cm^2, depending on the number of beams and their incidence angle.

The primary diagnostics used during this experimental campaign were the VISAR[14] and the SOP.[15] Due to the fact that the shocked states are very hot ($\gtrsim$1 eV), the shocked material has a significant population of free electrons and readily emits in the near-infrared, optical, and ultraviolet portions of the spectrum. The VISAR records the time evolution of the Doppler shift of a probe laser that results from the advancing reflective shock-wave front. With the measurement of the shock-wave velocity in the reference material (or witness) and the target, the pressure and density of the shocked material can be determined with the impedance-matching technique. The SOP records the time evolution of the shock emission, which can then be related to a Planck radiation source to determine the temperature of the shock front. Using these diagnostics it is possible to fully capture the EOS of a shocked material.

The VISAR and the SOP share a common telescope located on the experimental axis directly opposite the OMEGA beams used to launch the shock wave into the sample (see Fig. 111.18). The telescope includes a mechanical assembly that allows the *in-situ* pointing and focusing of the diagnostics on the experimental package. The probe beam and the self-emission from the shock are relayed from the target, and a dichroic beam splitter separates the VISAR probe beam from the rest of the self-emission. Both the VISAR probe beam and the self-emission are relayed to the front of streak cameras that provide two-dimensional records. One dimension corresponds to a slit view of the relayed image, and the second dimension corresponds to a time sweep of that slit view. The spatial information from the slit allows the records from these diagnostics to be used to obtain shock evolution on complex targets with more than one region of interest.

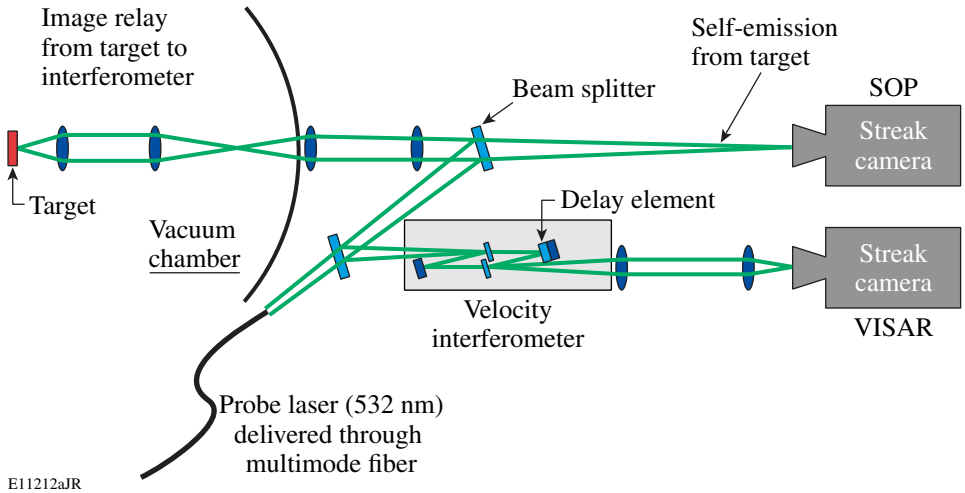

Figure 111.18
Basic configuration of the VISAR/SOP system on OMEGA. VISAR: velocity interferometer system for any reflector; SOP: streaked optical pyrometer.

Figure 111.19 shows side-by-side VISAR and SOP records that are representative of the data taken for this study. In the case of this experiment, OMEGA shot 37190, experimental records from an optically transparent, quartz/Ta_2O_5 aerogel target (image in Fig. 111.20) are shown. The two diagnostic records are displayed as two-dimensional, gray-scale density plots with the brightest regions being darkest. Time zero is the point at which the OMEGA drive beams begin to irradiate the target. Variations in the gray scale are related to shock evolution, showing that the material reflectivity (VISAR record) and the brightness (SOP record) are not constant. The two main contributors to this behavior are shock strength and the local material properties. The shock strength affects the quantity and energy of the free electrons, and the material properties dictate the scattering of light. The relative location of the fringes on the VISAR record corresponds to the shock velocity. The shock brightness temperature corresponds to the intensity of the SOP record.

The targets used in this study consist of a pusher assembly (a plastic ablator and an aluminum or quartz reference) that transmits a shock wave into a low-density aerogel sample (silica or Ta_2O_5) that is under study. These targets are generally 3-mm square, and the aerogel targets are transparent to optical wavelengths (Fig. 111.20). The targets are mounted on stalks and oriented such that the OMEGA beams are incident symmetrically about the target normal and the two principal diagnostics (VISAR and SOP).

The reference assembly has two components: a plastic ablator and a reference material. The plastic ablator is a 20-μm-thick foil of polystyrene (CH) that is irradiated by the laser.

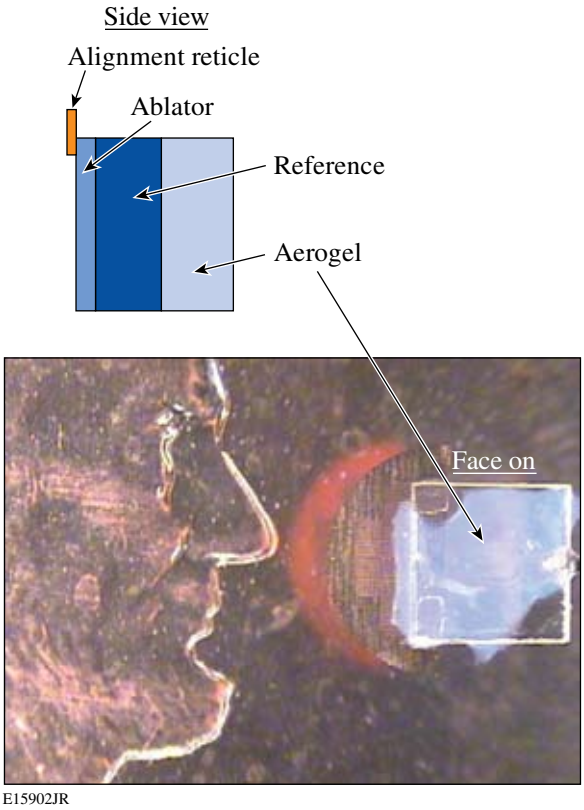

Figure 111.20
A typical Ta_2O_5 aerogel, planar target with a plastic ablator and quartz reference shown relative to a penny. These targets are generally 3×3-mm slides attached to a mounting stalk. This view shows the target as seen from the diagnostics (VISAR and SOP). The backing is a combination of a plastic ablator and a quartz slide, and the light amorphous material is the aerogel. Target alignment reticles, the grid to the left of the sample, are used to aid in pointing, rotation, and focusing during the experiment.

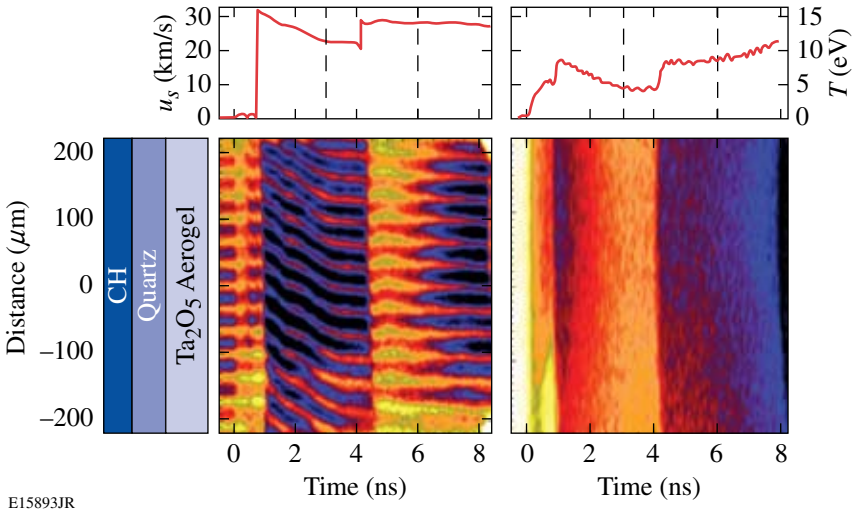

Figure 111.19
The target cross-section is depicted on the left. The VISAR (left plot) and SOP (right plot) records for OMEGA shot 37190 give simultaneous records of the evolution of shock velocity and shock temperature along with the associated inferred velocity and temperature profiles for a 12-beam, 1.9-TW/cm^2 shot on a quartz reference Ta_2O_5 aerogel target. Each lineout is taken at position zero in the records, which corresponds to the same point on the target.

Polystyrene is commonly used as the ablator due to its low atomic number [which reduces the production of high-energy (>2 keV) x rays] and its ease of handling and machining. Lower-energy x rays are more easily absorbed in the dense, highly ionized, shocked ablator, keeping x rays away from the reference and the target and minimizing the preheat of the materials before the shock arrives. The ablator thickness is chosen to be about twice the ablation depth of the laser to ensure that none of the higher-atomic-number reference material is heated by the laser while minimizing the amount of time the shock propagates through the ablator. The ablator is attached to the reference material using a UV-cured epoxy.

The two reference materials used in this study were aluminum and *z*-cut alpha quartz. The aluminum pushers were approximately 70 μm thick while the alpha-quartz thicknesses were 100 μm thick to compensate for the slightly lower x-ray absorption in the quartz. The aerogels were mounted to the aluminum reference by bonding a freestanding aerogel sample onto an aluminum foil. To ensure that the glue did not wick into the aerogel, the samples were glued only at the edges, again with the UV-cured epoxy. The consequence of gluing the aerogel to the aluminum was that gaps, owing to the surface roughness of the aerogel, were present between the reference and the target. These gaps increase the uncertainty in the selection of the proper isentrope (initial state) for the release wave. With the alpha-quartz pushers the aerogel was grown directly onto the pusher, eliminating the gaps at the contact surface. This manufacturing technique was possible because, while the aluminum would disintegrate in the environment of the aerogel manufacturing process, the alpha quartz was unaffected.

Tantalum pentoxide, in its standard state, is a white to creamy-white solid with a density of ~8.2 g/cm^3. The material has a relatively large band gap of ~4.2 eV, a high index of refraction (~2.1 at 532 nm), low absorption of optical and IR wavelengths (300 nm to 2 mm), and a low melting point (~1800 K, as compared to pure Ta, ~2700 K). The Ta_2O_5 aerogel in this study had three mean densities: 0.1, 0.15, and 0.25 g/cm^3. Since the aerogel grains are of the order of 2- to 50-nm scale, much less than the wavelength of light, a significant amount of Rayleigh scattering occurs within these aerogels. This limits the maximum sample thickness that can be probed with optical diagnostics to a few-hundred micrometers for 0.1-g/cm^3 aerogel and approximately 100 μm for the 0.25-g/cm^3 aerogel.

The Ta_2O_5 aerogels were produced by the Target Fabrication Group at Lawrence Livermore National Laboratory via a sol-gel process that entails the hydrolysis of tantalum ethoxide [$Ta(OC_2H_5)_5$] in an ethanol solution.[17] The targets are grown by dip-coating quartz slides in the gelatinous solution. They are then placed in a casting vessel for supercritical extraction of the ethanol. While in the solution and during the extraction of the ethanol solvent, the tantalum atoms bond with oxygen atoms, forming primarily Ta_2O_5 molecules. Unbonded surface oxygen atoms may terminate in either a hydroxol or an alkynol (typically methanol) group. If the aerogel is sintered after the drying process, the alkyl groups will be released, leaving only hydroxyl groups, which greatly increases the water absorptivity of the aerogel. Samples studied with an aluminum reference are then removed from the quartz and bonded to the reference assembly. Quartz-referenced targets merely require affixing the plastic ablator on the quartz slide.

Porous aerogels are hydrophilic, readily absorbing atmospheric moisture, which is physiosorbed (held by Van der Waals forces). The high polarizability of the hydroxyl groups as compared to an alkyl group makes the sintered materials especially hydrophilic, making it difficult to remove all of the moisture from the sample. Most experiments with a Ta_2O_5 aerogel (including this study) use unsintered samples, so that these aerogels have residual alkyl groups that are weakly chemically bound, or chemisorbed, to the surfaces of the aerogel structures. Combustion analysis puts the mass percentage of carbon at 1% or less, which is interpreted as a chemically absorbed contaminant that is present during all unsintered studies with this material.

The aerogel targets used in this study were produced by creating a "vat" of the catalyzed tantalum ethoxide/ethanol solution as described above. The samples were formed on quartz slides by coating them with the gelatin and placing the slide in a casting vessel. The manufacturer casts a much larger witness from the same vat that is machined and weighed for density estimates. These growth techniques are expected to be highly reproducible with manufacturer-quoted density errors of less than 10%. A systematic densification of the samples (compared to the witness) is possibly due to an increase in the importance of capillary effects for the large-aspect-ratio targets.

Experimental Observations

In this section, the series of measurements required to determine the EOS of the Ta_2O_5 aerogel will be discussed. The measurements can be subdivided into two categories: (1) characterization of the targets and the reference and (2) the actual target experiments.

The characterization measurements provide input so that the target experiments can be evaluated. They include the refractive-index characterization (needed to determine shock velocity), the density characterization (needed for the impedance-matching technique), and the quantification of manufacturing residuals (needed to verify the manufacturer's estimate). The refractive index was measured as an input to the shock-velocity measurements, and this value helped evaluate density measurements. To determine the amount of absorbed contaminants removed prior to an experiment, a series of experiments were performed that exposed aerogel samples to heat and vacuum to determine the quantity and type of contaminants for comparison with the manufacturer's estimates.

With the characterization of the target and the reference materials established, the necessary inputs are available for interpreting experimental observations of the EOS of Ta_2O_5. The observations include kinematic properties, which can be determined by measuring the shock velocities with VISAR, and the thermal properties, which can be determined by measuring the shock brightness with the SOP.

1. Refractive-Index Measurements of the Ta_2O_5 Aerogel

The refractive index n of the sample material affects the VISAR sensitivity,[14] and due to the highly porous nature of aerogels, the optical properties of an aerogel material differ greatly from its standard amorphous state. For these aerogels, the real part of the refractive index is near unity and the imaginary part is negligible.[18] Due to this near-unity refractive index and the thinness of these aerogel samples, it was necessary to use an optical technique based on white-light interferometry to measure the refractive index of the targets.[19] This technique uses the short coherence length of white light to identify the apparent depth of a reflective surface that is viewed through a refractive medium of thickness d, as shown in Fig. 111.21(a). This depth adjustment ΔL achieves a total optical path length (OPL*) through the sample that is equal to the OPL from the reflective surface through air. Using these two positions to eliminate the unknown distance between the image plane and the surface of the refractive medium, a relationship among these quantities is obtained:

$$\mathrm{OPL} - \Delta L - d = \mathrm{OPL}^* - nd \ , \tag{1}$$

and after solving for n, the simple relation

$$n = 1 + \Delta L / d \tag{2}$$

is found, where n is the real part of the index of refraction.

A ZYGO NewView 5000 white-light interferometer,[20] was used to measure both the depth adjustment ΔL due to the refractive property of the aerogels and the thickness of the aerogels. The objective numerical aperture (N.A.) for the ΔL measurement was 0.075 to keep the incident rays as normal to the aerogel surface as possible. The thicknesses d of the aerogel targets were measured in the manner shown in Fig. 111.21(b). Because the refractive index for these aerogels is close to that of air and the surface of the aerogel has a surface roughness of the order of a few microns, the thickness measurements required the use of an objective with a N.A. of 0.33 to achieve a small depth of focus. The use of this relatively large N.A. limited the overall depth of field to about a millimeter. Through multiple measurements around the edge, a reasonable surface profile was obtained. The uncertainty in the ΔL measurement was dominated by the need to use a small N.A. objective that had a depth of focus of about 0.1 μm, resulting in an uncertainty of ΔL at about 4%, while the uncertainty in identifying the thickness d of the target was approximately 3%. The refractive indices of the Ta_2O_5 aerogel targets were measured to be 1.0206±0.0010, 1.0297±0.0017, and 1.0471±0.0024 for the 0.1-, 0.15-, and 0.25-g/cm^3 aerogel targets, respectively.

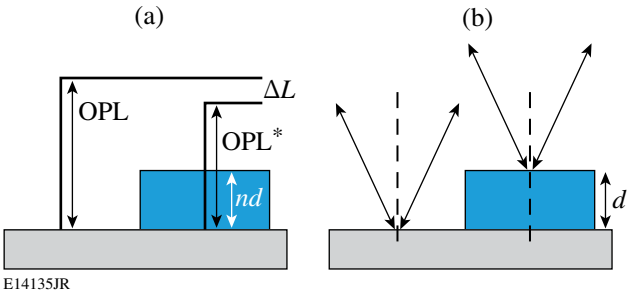

Figure 111.21
The measurement technique that determined the refractive index included two steps: First, the change in stage position, ΔL, required that the base of the sample be kept at an equal optical path length (OPL) through air and the target (a). Second, the thickness of the sample was measured by the difference d in stage position for the target's upper surface in focus position and the base in focus position (b). Because the measurement (a) is through the sample, a small N.A. is desirable, whereas a large N.A. works best for the surface measurement of (b).

2. Density Measurements of an Ta_2O_5 Aerogel

The nominal initial density values of 0.1, 0.15, and 0.25 g/cm^3 supplied by the manufacturer were estimates based on a witness sample rather than the actual sample itself. To determine if the target densified more than the witness during the drying process, it was deemed necessary to validate the provided estimates. These microscopic samples were validated by relating the density to the refractive index of the target.

The Claussius–Mossotti relation[21] applied to a highly porous material shows that the refractive index n less unity is proportional to the density ρ of the porous material:

$$n - 1 = \alpha\rho, \tag{3}$$

where α is a proportionality constant associated with the strength of the dipole oscillators.[18] Knowing this proportionality constant and the refractive measurements discussed in **Refractive-Index Measurements of the Ta_2O_5 Aerogel** (p. 158), the density of the actual target materials can then be determined. To ascertain the proportionality constant, the manufacturer machined a witness sample of known density to approximately 100 μm thick. At this thickness, the technique described on p. 158 was used to determine the refractive index. Based on such measurements, the proportionality constant was determined to be 0.188±0.013. Using this result, it was found that the densification of the targets compared to the witness sample is less than the combined uncertainties of the measurements of the refractive index and the proportionality constant; thus, the density of the witness accurately reflects that of the target. This equality provides no information on the purity of the samples, or what contaminants, such as water or alkyls, are present in a target. To resolve the amount of the residuals, another set of measurements was required to quantify the amount of contaminants absorbed and the nature of their bonding mechanisms.

A series of three tests were run on samples from the same batch of Ta_2O_5 aerogel in ambient laboratory air having 30% to 40% relative humidity. The samples were approximately 0.5 cm in diameter, roughly 2 cm in height, and weighed approximately 100 mg prior to testing. The first test determined the total amount of residuals by heating the sample in a dry nitrogen atmosphere utilizing a Computrac moisture analyzer.[22] The samples were heated to 450 K over approximately 5 min based on the analyzer's termination criteria, then removed from the analyzer and transferred to a scale capable of 0.1-mg-accuracy measurements. The mass of the sample and absorbed moisture was tracked as a function of time after its initial exposure to air. Because of the need to transfer from the test apparatus to a scale, the measurement began ~15 s after initial exposure. Figure 111.22 shows the measured time-dependent aerogel and absorbed contaminant mass after exposure to atmosphere. Extrapolating these results to time zero, the mass of the target without any contaminants was inferred to be 100.8±0.1 mg. The measured initial mass (prior to heat exposure), 104.7±0.1 mg, was then normalized to this extrapolated value to determine the mass percentage of

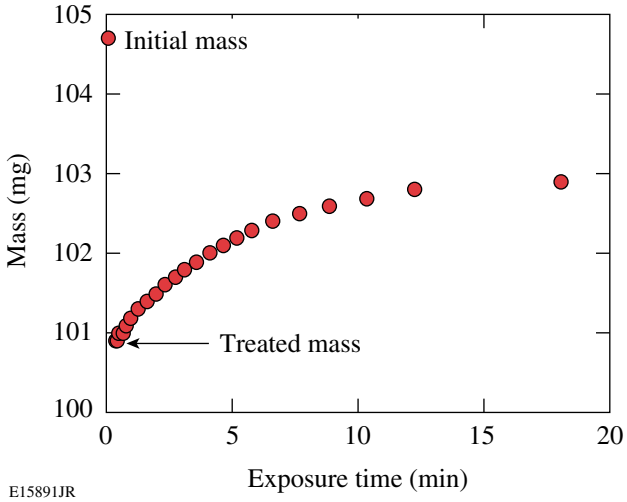

Figure 111.22
A characteristic plot of the total mass of a sample with absorbed water as a function of time after removal from the heat-addition test. Three such tests were performed: this first test was performed to measure the full chemically and physically absorbed contaminants, a second to determine the amount of physically absorbed contaminants, and a third to determine the amount of physically absorbed contaminants removed in an OMEGA shot cycle.

contaminants, which constitutes about 4% of the mass of the sample as it came from the manufacturer. The second sample was exposed to a vacuum (~10^{-4} Torr), however, with no heat addition. This sample remained in a vacuum environment for a week and was then removed and measured in the same manner as previously described. After normalization, it was found that approximately 3% of the as-manufactured mass is due to absorbed contaminants that can be removed by vacuum alone. To determine if the normal OMEGA shot cycle, which is approximately 20 min of vacuum exposure, achieves the same result, a third sample was placed in an equivalent vacuum for a period of 20 min and then removed and measured in time. The extrapolation of this sample again showed that the mass percentage of physiosorbed contaminants removed was 3% of the total as-manufactured mass.

These measurements indicate that approximately 1% of the as-manufactured mass fraction is from chemisorbed contaminants (contaminants that require heat addition to break bonds), while the remaining 3% is physiosorbed and sufficient for vacuum removal. Correlating these results with the manufacturer's carbon estimates based on combustion analysis experiments, it is expected that the chemisorbed contaminants are the alkyls and that the primary physiosorbed contaminant is absorbed water. The importance of these measurements is that the contaminants that can be removed by vacuum are removed

in times less than the OMEGA shot cycle; however, a small amount of the residual alkyl groups are present in experiments using this aerogel.

3. Kinematic Properties of Ta_2O_5 Aerogel

The kinematic properties of the Ta_2O_5 aerogel samples were studied using both aluminum and alpha quartz as reference materials. The shock velocity in the aluminum reference was inferred from a quartz witness adjacent to the aerogel sample, as shown in Fig. 111.23, following the high-precision method proposed by Hicks *et al.*[6] In this study, the linear relationship, reported by Hicks *et al.*, between the measured shock velocity in a quartz witness and the shock velocity in aluminum, $u_s^{\mathrm{Al}} = B_0 + B_1\left(u_s^{\mathrm{Q}} - \overline{u_s^{\mathrm{Q}}}\right)$, where $\overline{u_s^{\mathrm{Q}}} = 20.57\ \mu\mathrm{m}/\mathrm{ns}$, $B_0 = 21.14 \pm 0.12\ \mu$m/ns, and $B_1 = 0.91 \pm 0.03$, was used to determine the aluminum shock velocity. The shock velocities in both the quartz and aerogel portions of the sample were determined with VISAR and are tabulated in Table 111.III along with the other kinematic parameters determined from the impedance-matching analysis using the SESAME-3700 equation-of-state model for aluminum.

Although aluminum is a proven reference material, the difficulties of affixing these aerogels to the aluminum contact surface without gaps proved to be challenging and had a low success rate; consequently, the target design was switched to the quartz reference similar to that shown in Fig. 111.24 with Ta_2O_5 aerogel across the entire target. With the aerogel grown directly on the reference, the interface between the two materials was gapless, leading to a perfect shot success rate. With the quartz pushers and transparent aerogels, the shock velocity was continuously measured through the quartz pusher and into the aerogel. Table 111.IV lists the 19 experimental results, u_s^{Q} and $u_s^{\mathrm{Ta_2O_5}}$, for the aerogels of the three nominal densities along with the particle velocity and pressure inferred from the impedance-matching technique using the Kerley-7360 model.

Figure 111.25 shows the results for the shock-velocity dependence on the particle velocity for the three different densities of Ta_2O_5 aerogel (the initial densities 0.1-, 0.15-, and 0.25-g/cm^3 targets are solid diamond, open ellipses; solid diamond, gray ellipses; and open diamond, solid ellipses, respectively). Experiments with the 0.25-g/cm^3 aerogels were performed with both aluminum and alpha-quartz pushers. In Fig. 111.26, these points are translated into the pressure-density equation-of-state plane, with the same designations. Also shown in Fig. 111.26 are the *a priori* predictions by the qEOS model for this material (shown with the open, gray, and solid curves correlating to 0.1, 0.15, and 0.25 g/cm^3 as with the measurements). Figure 111.26

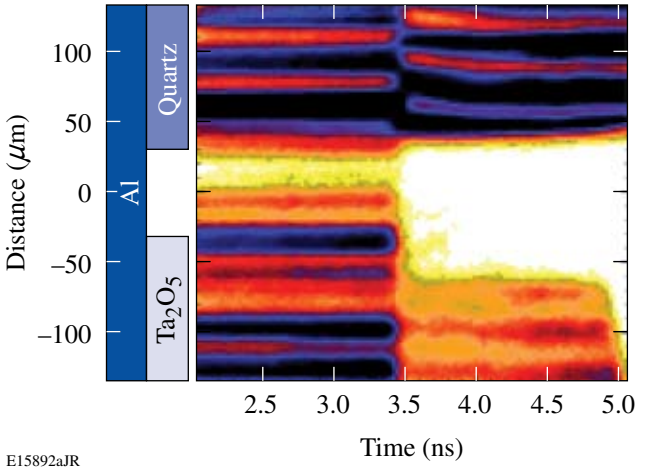

Figure 111.23
The experimental package used when the reference material is aluminum includes a quartz witness material in addition to the aerogel. The interferogram shows the shock within the aerogel (lower half) and within the quartz (upper half). Before 3.5 ns, the shock is within the aluminum reference. After 3.5 ns, the shock reaches the material interface where it breaks out of the aluminum. The quartz and aerogel shock velocities are both determined within 1 ns of the breakout.

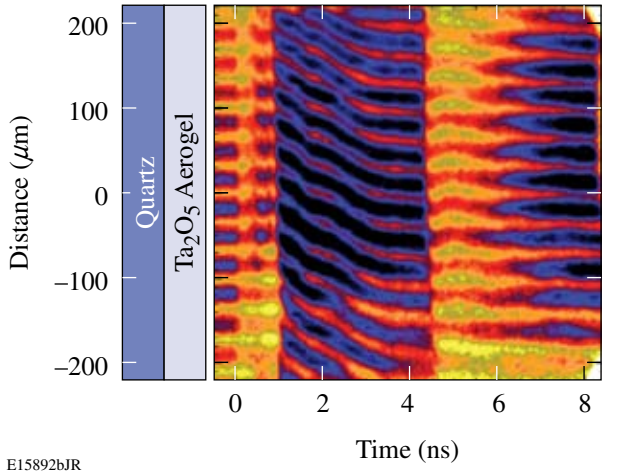

Figure 111.24
The target and VISAR data with a quartz pusher are shown. The interferogram from an experimental record shows the shock evolution as it propagates through the target. At $t = 0$, OMEGA begins irradiating the surface of the target. At approximately 1 ns, the shock exits the plastic ablator and enters the quartz with a reflected shock going back into the ablator. Due to the expansion of the critical surface, the coupling between the laser and the target decreases, resulting in a decay in the strength of the shock as evidenced by the fringe movement. At $t = 3.5$ ns, the shock is strengthened by the arrival of a compression wave due to the arrival of the reflected shock at the vacuum interface. This causes the shock wave to become steady as it approaches the interface. The shock reaches the interface at 4.5 ns. In this example, the shock velocity for the quartz is determined between 3 to 4.5 ns and for the aerogel between 4.5 to 6 ns.

Table 111.III: Ta_2O_5 aerogel-aluminum impedance matching.

Shot number	$\rho_0^{Ta_2O_5}$ (g/cm^3)	u_s^{Al} (μm/ns)	P^{Al} (Mbar)	$u_s^{Ta_2O_5}$ (μm/ns)	u_p μm/ns)	$P^{Ta_2O_5}$ (Mbar)	$\rho^{Ta_2O_5}$ (g/cm^3)
34136	0.25±0.025	24.6±0.3	10.1±0.3	30.6±0.5	25.3±0.7	1.94±0.18	1.46±0.24
34138	0.25±0.025	19.1±0.3	5.5±0.2	21.7±0.5	18.3±0.6	0.99±0.11	1.58±0.38
34141	0.25±0.025	25.5±0.3	11.0±0.3	32.2±0.5	26.5±0.7	2.13±0.19	1.40±0.22
34143	0.25±0.025	24.1±0.3	9.6±0.3	30.0±0.5	24.7±0.6	1.85±0.17	1.41±0.23
34915	0.25±0.025	27.1±0.3	12.6±0.3	35.1±0.5	28.4±0.7	2.50±0.22	1.32±0.18
34917	0.25±0.025	22.0±0.3	7.8±0.25	26.5±0.5	22.0±0.6	1.46±0.14	1.48±0.26
35152	0.25±0.025	26.3±0.3	11.7±0.3	33.5±0.5	27.4±0.7	2.30±0.21	1.38±0.21
35153	0.25±0.025	25.9±0.3	11.4±0.3	32.4±0.5	27.0±0.7	2.19±0.20	1.51±0.25
34136	0.25±0.025	24.6±0.3	10.1±0.3	30.6±0.5	25.3±0.7	1.94±0.18	1.46±0.24

Shot data and inferred EOS parameters of Ta_2O_5 aerogel. The columns correspond to the OMEGA shot archive number, the initial density of the aerogel, the inferred shock velocity within the aluminum, the final shock strength prior to the wave decomposition, the shock velocity measured within the aerogel, the particle velocity that conserves mass and momentum for the wave decomposition, the strength of the shock within the aerogel, and the density of the shocked compressed aerogel.

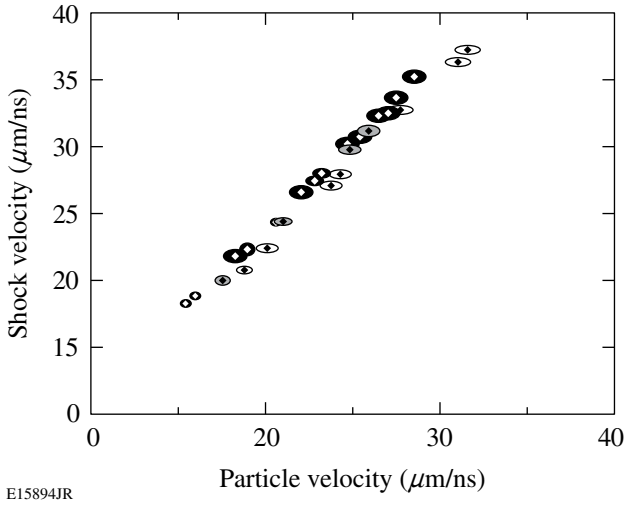

Figure 111.25
The shock-velocity dependence on the particle velocity for the three densities of this study. The points with the open error ellipses and gray error ellipses are from the 0.1- and 0.15-g/cm^3 aerogels, respectively. Experiments in 0.25-g/cm^3 aerogels (solid ellipses) used aluminum references and quartz references. The uncertainty of the velocity measurements was dramatically reduced with the quartz reference as evidenced by the relative area of the error ellipses.

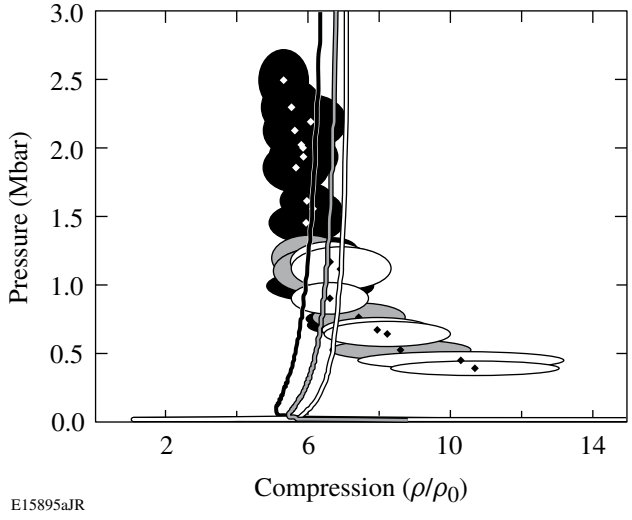

Figure 111.26
The translation of the u_s–u_p plane to the shock strength versus the compressed-density plane for the three densities: 0.1, 0.15, and 0.25 g/cm^3 (open, gray, and solid, respectively). In addition to the measurements, the qEOS model's predicted dependence for the three densities is shown as the solid lines. As can be seen, below 1 Mbar the measured compressed density is significantly higher than that predicted; however, above 1 Mbar, the qEOS model appears to adequately predict the material behavior.

Table 111.IV: Ta_2O_5 aerogel-quartz impedance matching.

Shot number	$\rho_0^{Ta_2O_5}$ (g/cm^3)	u_s^Q (μm/ns)	P^Q (Mbar)	$u_s^{Ta_2O_5}$ (μm/ns)	u_p (μm/ns)	$P^{Ta_2O_5}$ (Mbar)	$\rho^{Ta_2O_5}$ (g/cm^3)
37190	0.10±0.01	21.2±0.2	7.4±0.15	27.0±0.3	23.7±0.6	0.64±0.09	0.82±0.18
37729	0.10±0.01	26.8±0.2	12.4±0.2	37.1±0.3	31.5±0.7	1.17±0.15	0.66±0.11
37730	0.10±0.01	18.5±0.2	5.5±0.1	22.3±0.2	20.1±0.5	0.45±0.06	1.03±0.29
37731	0.10±0.01	17.6±0.1	4.9±0.1	20.7±0.2	18.8±0.3	0.39±0.05	1.07±0.24
37732	0.10±0.01	21.6±0.2	7.7±0.2	27.8±0.3	24.3±0.6	0.68±0.09	0.79±0.16
37734	0.10±0.01	24.1±0.2	9.8±0.2	32.6±0.2	27.7±0.6	0.90±0.12	0.66±0.11
38790	0.10±0.01	26.4±0.3	12.0±0.3	36.2±0.3	31.0±0.8	1.12±0.15	0.69±0.14
38127	0.15±0.015	17.3±0.1	4.7±0.1	19.9±0.3	17.6±0.4	0.53±0.07	1.29±0.30
38129	0.15±0.015	19.9±0.2	6.4±0.1	24.3±0.2	21.0±0.5	0.77±0.10	1.11±0.20
38793	0.15±0.015	23.6±0.2	9.4±0.2	31.0±0.4	25.8±0.6	1.20±0.16	0.90±0.16
38794	0.15±0.015	22.8±0.2	8.7±0.2	29.7±0.3	24.8±0.6	1.10±0.15	0.90±0.15
36542	0.25±0.025	19.2±0.2	6.0±0.1	22.2±0.4	19.0±0.4	1.05±0.09	1.72±0.31
36545	0.25±0.025	24.8±0.2	10.5±0.2	31.1±0.4	25.8±0.5	2.00±0.16	1.46±0.19
36546	0.25±0.025	22.7±0.2	8.6±0.2	27.9±0.3	23.2±0.5	1.62±0.13	1.48±0.19
42092	0.25±0.025	16.5±0.1	4.2±0.1	18.2±0.2	15.5±0.3	0.71±0.06	1.70±0.22
42094	0.25±0.025	16.9±0.1	4.4±0.1	18.8±0.2	16.0±0.3	0.75±0.06	1.70±0.22
42097	0.25±0.025	24.9±0.1	10.6±0.1	31.3±0.2	25.9±0.3	2.03±0.14	1.44±0.13
42098	0.25±0.025	20.6±0.1	6.9±0.1	24.3±0.2	20.7±0.3	1.26±0.09	1.67±0.18
42099	0.25±0.025	22.4±0.2	8.4±0.2	27.3±0.3	22.8±0.4	1.56±0.13	1.53±0.20
37190	0.10±0.01	21.2±0.2	7.4±0.15	27.0±0.3	23.7±0.6	0.64±0.09	0.82±0.18

Shot data and inferred EOS parameters of Ta_2O_5 aerogel. The columns are arranged as in Table 111.III.

shows that the model predicts the observed local asymptote at approximately six-fold compression for a strong shock. A disagreement exists at the lower pressures ($\lesssim$Mbar) where the experiments exhibit higher compression than predicted by the model. The model's region of high compression, occurring at ~0.10 Mbar, is at much lower shock strength than that found in these experiments.

The shock velocities across the contact surface are used with the impedance-matching technique to derive the kinematic properties of the shock. This procedure is shown in Fig. 111.27 for OMEGA shot 37190. The shock velocity in the quartz just prior to the shock arrival at the contact surface is 21.2 μm/ns with an uncertainty of ~1% because the contact surface is free of gaps. This yields a Rayleigh line with a slight slope uncertainty. The intersection of the Rayleigh line and its uncertainty lines with the reference Hugoniot (in this case quartz) identifies the release shock state P_0 with its associated uncertainty. The isentropes from P_0 and its uncertainty are calculated for the reflected wave. These isentropes are matched to the Rayleigh line for the aerogel, the product of 0.1 g/cm^3 and 27 μm/ns, with the associated uncertainty in this slope, ~10%. The uncertainties in the final kinematic parameters reported in this study were reported as the larger of the uncertainties in the matched

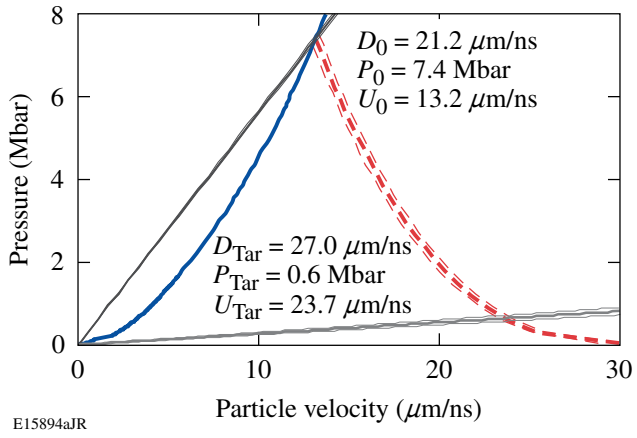

Figure 111.27
Uncertainties in the slopes of the Rayleigh lines were used to determine the uncertainties in the kinematic properties for shot 37190. The uncertainty in the measurement of the shock velocity of the reference standard produces uncertainties in the isentrope (dashed curves), which combines with the uncertainties in the density of the aerogel and shock velocity in the aerogel (thin, light gray curves).

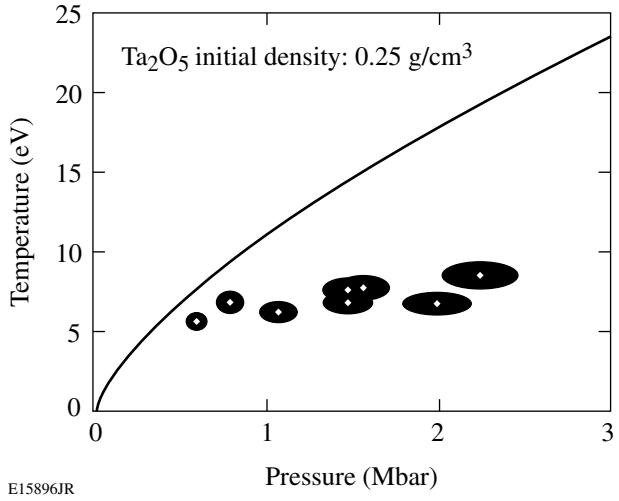

Figure 111.28
The temperature dependence on the shock strength for the 0.25-g/cm^3 aerogel shows that the predicted temperature for qEOS is significantly different than that observed. Above 0.1 Mbar the rise in predicted temperature as the shock strength increases is about three times greater than the observed temperature dependence on shock strength.

values, i.e., $\delta u_p = \max\left[\left\{\delta u_{p\_}, \delta u_{p+}\right\}\right]$, $\delta P = \max\left[\left\{\delta P\_, \delta P_+\right\}\right]$.

4. Thermal Properties of Ta_2O_5 Aerogel

The streaked optical pyrometer was used to infer the brightness temperature of the shock front. These measurements involved the simultaneous measurement of the shock velocity and its brightness just prior to the shock's arrival at the rear surface. Brightness measurements are acquired just before shock breakout to eliminate uncertainties in the shock-front brightness that might occur due to the scattering or absorption of light within the unshocked target ahead of the shock. The dependence of brightness and shock-velocity measurements are translated to temperature dependence on shock pressure using the NIST-traceable calibration of the SOP[15] and the kinematic measurements discussed in **Kinematic Properties of Ta_2O_5 Aerogel** (p. 160), respectively. The results for the 0.25-g/cm^3, Ta_2O_5 aerogel are shown in Fig. 111.28 along with the prediction by qEOS (solid line). As can be seen in this figure, the qEOS model overpredicts the temperature of the shock front. In the strong-shock limit [temperature (T) $\propto$ shock strength (P)], the slope of the locus of points, $(\Delta T/\Delta P)_{Hug}$, is a few times greater than that of the measured values.

Discussion

The measurements of the EOS of the Ta_2O_5 showed marked differences to the *a priori* qEOS model that has been built for the material. It was shown that the qEOS model exhibits very different behavior in the sub-Mbar regime than the measurements. In this shock-strength regime, the qEOS model behavior is much stiffer (small compression for given shock strength) than that observed experimentally. High temperatures with only translational degrees of freedom available would restrict the final compression to this extent, so it is necessary to look at the Ta_2O_5 molecule to see if there may be neglected degrees of freedom to account for this deviation. While the temperature measurements could be consistent with the higher compressions in experiment (as opposed to those found with qEOS), the temperature's very weak dependence on shock strength suggests consideration of other potential reasons.

In **qEOS Kinematic Agreement** (p. 164), the Ta_2O_5 aerogel measurements will be compared with SiO_2 aerogel measurements conducted at multiple laboratories. The silica aerogels have a comparable final density to the Ta_2O_5 aerogels; however, they exhibit marked differences in some of their fundamental properties, namely the binding energy. Due to the finite time required for ionization, the possibility of nonequilibrium between the free electrons and the ions will be considered in **qEOS Thermal Properties** (p. 164). While this nonequilibrium would adversely affect thermal measurements that rely on the local electron temperature near the critical surface of the SOP, it would not affect the kinematic measurements, which

rely on an equilibrium wave that is much less localized.

1. qEOS Kinematic Agreement

The shock-strength dependence of the compression for silica aerogel and Ta_2O_5 is shown in Fig. 111.29. Based on the Ta_2O_5 response, the Thomas-Fermi–based qEOS model [lines in Fig. 111.29(b)] is in good agreement with the high-pressure, kinematic behavior of Ta_2O_5. This agreement begins approximately between 0.75 and 1 Mbar for the three studied aerogel sample densities. The agreement at higher pressure means that sufficient ionization exists to allow the free electrons in the plasma to dominate the kinematic behavior of the background molecules/ions. At low pressure, the difference between the predicted and observed response is large, with predicted compression ratios far lower than those experimentally observed. This behavior indicates that the qEOS model is probably handling the dissociation of the material incorrectly. This is consistent with a reduction in the observed temperature.

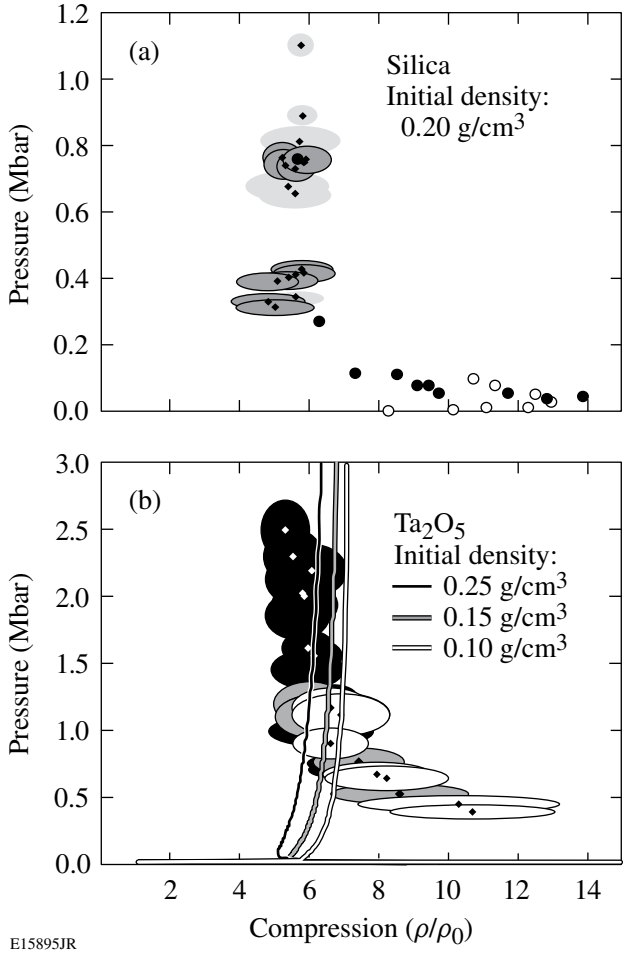

Figure 111.29
These two graphs show the shock-strength dependence of the compression for (a) silica aerogel and (b) the Ta_2O_5 aerogel. The data and curves in both (a) and (b) exhibit high compressions at low pressures due to molecular contributions to the material compressibility. The molecular contributions become negligible at about 0.3 Mbar in the silica aerogel and at about 0.1 Mbar in the Ta_2O_5 aerogel. Above these threshold values, the compression is essentially independent of shock strength. The silica data are from Boehly *et al*. (light gray ellipses), Knudson *et al*. (dark gray ellipses), Trunin and Simakov (solid circles), and Vildanov *et al*. (open circles).[13,23–26]

When comparing the Ta_2O_5 aerogel to the silica aerogel, it is clear that there is precedent for this increased compressibility relative to qEOS predictions for these two materials, which are of comparable final density. The main difference between this Ta_2O_5 study and the studies in the silica aerogel is that the pressure at which the Ta_2O_5 aerogels exhibit compression independence is about three times higher than that in the silica aerogel. Ta_2O_5 has a total sublimation/dissociation energy[26] of

$$Ta_2O_5(s) \rightarrow 2\,Ta(g) + 5\,O(g); \qquad \Delta H_0 = 1157\ \text{kcal/mol}, \tag{4}$$

which is approximately three times larger than that of SiO_2 (Ref. 27):

$$SiO_2(s) \rightarrow Si(g) + 2\,O(g); \qquad \Delta H_0 = 443\ \text{kcal/mol}. \tag{5}$$

This difference appears to account for the delayed onset of Thomas–Fermi behavior. The Ta_2O_5 remains more compressible because these molecular structures provide an increased compressibility through the additional degrees of freedom and higher energy consumption to break the bonds.

2. qEOS Thermal Properties

The disagreement between the qEOS model and the temperature measurements in **Thermal Properties of Ta_2O_5 Aerogel** (p. 163) is pronounced. The kinematic results indicate that the Ta_2O_5 material can absorb more energy than predicted by the qEOS model. The apparent independence of the measured temperature on the pressure suggests that local, nonequilibrium processes may also be important. Studies of other material have indicated that at sufficiently high pressures the brightness/temperature measurements in alkali halides (NaCl, KCl, and KBr) approached a similar plateau where the observed temperature became nearly constant with shock strength.[28] An explanation for these observations based on a lack of equilibrium between electrons and the atoms just behind

the shock front was provided by Zeldovich.[29] Zeldovich argued that the energy of a shock wave is carried by the atoms and transferred (via collisions) to the electrons; thus, full equilibrium depends on the rate of electron–ion collisions. In most crystalline materials, the collision frequency is sufficiently high that equilibration occurs on a subpicosecond time scale. If the shock speed is sufficiently high and the collision rates are moderate, then equilibration can lag significantly behind the shock-wave front. This would result in the electron temperature being lower than the ion temperature until deep into the shock front. As the electron temperature is equilibrating, ionization is taking place, resulting in an increase in electron density as a function of position within the shock. Consequently, if the critical surface of a pyrometer channel is closer to the observer than the equilibrium temperature, then the brightness temperature, which is predominantly related to bound-free and free-free electronic transitions, would be artificially low.

To determine if these aerogels exhibit this nonequilibrium behavior, a simulation of the experiment was performed using the one-dimensional hydrodynamics code HYDRA.[30] In this simulation, a 0.1-g/cm^3 sample of Yb_2O_5 was shocked by a quartz pusher in the same configuration as shown in Fig. 111.24. It should be noted that ytterbium (Yb) was used as a surrogate for Ta because opacity tables for Ta were unavailable at the time of the simulation. The simulated drive environment was identical to that used in OMEGA shot 37190. Figure 111.30(a) shows the predicted electron density $\left(n_e/n_c\right)$ as a function of the one-dimensional spatial coordinate in the simulation. The density is normalized to the critical density for the band of the SOP centered at 1.84 eV. Figure 111.30(b) shows the temperature of the electrons (dotted) and the ions (solid) as a function of the one-dimensional spatial coordinate in the simulation. As with density, the temperature is normalized to the electron temperature at the critical surface for the SOP measurement wavelength. These snapshots are from 7 ns after the laser pulse began and spatially referenced to the front surface of the ablator. In the density plot looking from left to right, the high-density shocked region, at positions less than 141 μm, is the advancing quartz pusher. The density gradient between 141 and 142 μm is due to the release of the high-density quartz into the lower-density, shocked aerogel. The measured shock-wave front is at approximately 145 μm and is a little over 500 nm thick. Ahead of the shock wave is a region where the radiation from the shock is ionizing some of the atoms in the unshocked material to ~4% of the equilibrium electron density of the shocked material. In the temperature plot, one can see the corresponding features behind the shock front. As one approaches the shock front, significant deviations

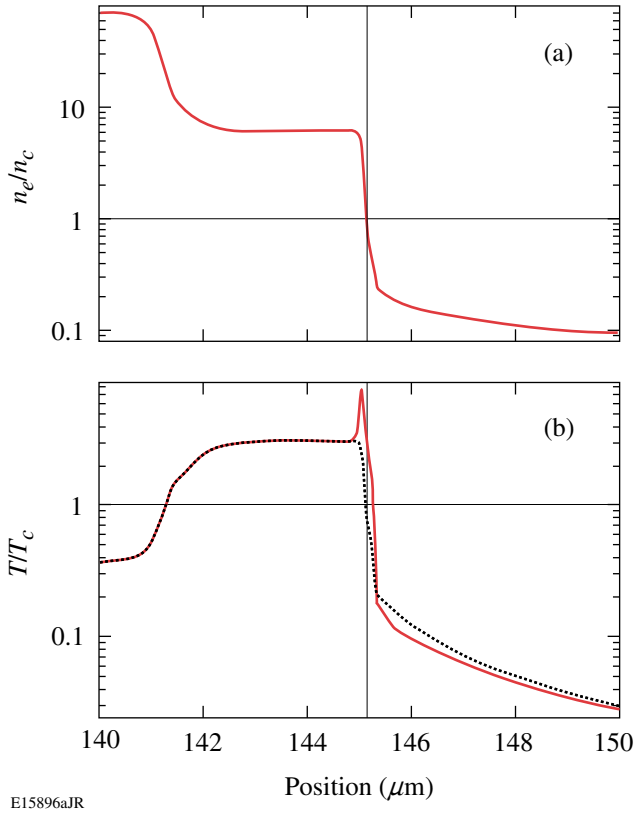

Figure 111.30
The electron density in the vicinity of the shock front (a) normalized to the critical density of the pyrometer's band center, 670 nm, and (b) the temperature of the electrons (dotted) and the ions (solid) in the vicinity of the shock front normalized to the electron temperature at the SOP's critical surface. In the position coordinate, up to 141 μm, the material is quartz, while from 142 μm and beyond, the material is the Yb_2O_5 aerogel. Between 141 and 142 μm, the quartz is releasing into the less-dense aerogel. From about 145 μm and beyond, the shock wave has not yet arrived; however, radiation from the shock front is ionizing and heating the nearby material in advance of the arrival of the shock. The actual shock front arrives at about 145 μm and rapidly heats the ions. The electrons come into equilibrium with the ions at about 0.5 μm behind the shock front.

occur between the electron and ion temperatures. The leading edge of the shock front transfers energy to the ions by ion–ion collisions, heating them very rapidly to a level above the final equilibrium value. The electron–ion collision cross section is much smaller; therefore the energy transfer to the electrons is much slower and lags behind the shock front.

The simulation indicates that the critical electron density for the measurement wavelength is achieved at a point ahead of where the electrons and the ions come into full equilibrium. Therefore, the measurement would exhibit lower temperatures than that produced by the shock wave. The most reasonable method to overcome this skin-depth issue is to observe the

shock at shorter wavelengths (i.e., at higher critical frequencies). For example, this simulation indicates that a 200-nm pyrometer would likely make an accurate measurement of the shock temperature.

Conclusions

This study provided experimental EOS data of highly porous Ta_2O_5 aerogels. Using the OMEGA Laser System, aerogel samples were compressed from their initial densities of 0.1, 0.15, and 0.25 g/cm^3 by shock waves with strengths between 0.3 and 3 Mbar. Under these shock loads, the materials were compressed to densities between 5 and 15 times their initial density and to temperatures ≥50,000 K. The shocked states as diagnosed with the VISAR and the SOP show strong deviations from the available qEOS model for this material. When the compression measurements are compared to qEOS, it is found that the model underestimates the level of compression achieved by shock loading below 1 Mbar but reproduces the material behavior above 1 Mbar. This observation indicates that there are material degrees of freedom below 1 Mbar that are not fully captured by the qEOS model. The thermal measurements indicate that this might be due to less-significant heating; however, the weak dependence of temperature on shock strength could indicate that nonequilibrium effects require more attention when considering aerogel materials.

ACKNOWLEDGMENT

This work was supported by the U.S. Department of Energy Office of Inertial Confinement Fusion under Cooperative Agreement No. DE-FC52-92SF19460, the University of Rochester, and the New York State Energy Research and Development Authority. The support of DOE does not constitute an endorsement by DOE of the views expressed in this article.

REFERENCES

1. R. Cauble *et al*., Astrophys. J. Suppl. Ser. **127**, 267 (2000).
2. G. W. Collins *et al*., Science **281**, 1178 (1998).
3. M. Koenig *et al*., Appl. Phys. Lett. **72**, 1033 (1998).
4. P. M. Celliers *et al*., Phys. Plasmas **11**, L41 (2004).
5. D. K. Bradley *et al*., Phys. Rev. Lett. **93**, 195506 (2004).
6. D. G. Hicks, T. R. Boehly, P. M. Celliers, J. H. Eggert, E. Vianello, D. D. Meyerhofer, and G. W. Collins, Phys. Plasmas **12**, 082702 (2005).
7. D. G. Hicks, T. R. Boehly, J. H. Eggert, J. E. Miller, P. M. Celliers, and G. W. Collins, Phys. Rev. Lett. **97**, 025502 (2006).
8. R. Cauble *et al*., Phys. Rev. Lett. **80**, 1248 (1998).
9. M. D. Knudson *et al*., Phys. Rev. Lett. **87**, 225501 (2001).
10. L. V. Al'tshuler, Sov. Phys.-Usp. **8**, 52 (1965).
11. C. A. Back *et al*., Phys. Plasmas **7**, 2126 (2000).
12. R. P. Drake, *High-Energy-Density Physics: Fundamentals, Inertial Fusion, and Experimental Astrophysics*, Shock Wave and High Pressure Phenomena (Springer, Berlin, 2006).
13. T. R. Boehly, R. S. Craxton, T. H. Hinterman, J. H. Kelly, T. J. Kessler, S. A. Kumpan, S. A. Letzring, R. L. McCrory, S. F. B. Morse, W. Seka, S. Skupsky, J. M. Soures, and C. P. Verdon, Rev. Sci. Instrum. **66**, 508 (1995).
14. P. M. Celliers, D. K. Bradley, G. W. Collins, D. G. Hicks, T. R. Boehly, and W. J. Armstrong, Rev. Sci. Instrum. **75**, 4916 (2004).
15. J. E. Miller, T. R. Boehly, A. Melchior, D. D. Meyerhofer, P. M. Celliers, J. H. Eggert, D. G. Hicks, C. M. Sorce, J. A. Oertel, and P. M. Emmel, Rev. Sci. Instrum. **78**, 034903 (2007).
16. Y. Lin, T. J. Kessler, and G. N. Lawrence, Opt. Lett. **20**, 764 (1995).
17. T. F. Baumann *et al*., in *Handbook of Porous Solids*, edited by F. Schüth, K. S. W. Sing, and J. Weitkamp (Wiley-VCH, Weinheim, Germany, 2002), p. 2014.
18. P. Wang *et al*., J. Phys. D: Appl. Phys. **27**, 414 (1994).
19. A. G. Van Engen, S. A. Diddams, and T. S. Clement, Appl. Opt. **37**, 5679 (1998).
20. Zygo NewView™ 5000, Zygo Corporation, Middlefield, CT 06455.
21. E. Hecht, *Optics*, 4th ed. (Addison-Wesley, Reading, MA, 2002).
22. Computrac Max-1000 moisture analyzer, Arizona Instruments, Phoenix, AZ 85040-1941.
23. T. R. Boehly, J. E. Miller, D. D. Meyerhofer, J. G. Eggert, P. M. Celliers, D. G. Hicks, and G. W. Collins, "Measurement of Release of Alpha Quartz: A New Standard for Impedance-Matching Experiments," submitted to the Proceedings of the APS.
24. M. D. Knudson, J. R. Asay, and C. Deeney, J. Appl. Phys. **97**, 073514 (2005).
25. G. V. Simakov and R. F. Trunin, Izv. Akad. Nauk SSSR Fiz. Zemli (11), 72 (1990).
26. V. G. Vildanov *et al*., in *Shock Compression of Condensed Matter '95, AIP Conference Proceedings 370*, edited by S. C. Schmidt and W. C. Teo (American Institute of Physics, Melville, NY, 1996), pp. 121–124.
27. M. G. Inghram, W. A. Chupka, and J. Berkowitz, J. Chem. Phys. **27**, 569 (1957).
28. J. D. Cox, D. D. Wagman, and V. A. Medvedev, *CODATA Key Values for Thermodynamics* (Hemisphere, New York, 1989).
29. S. B. Kormer, Sov. Phys.-Usp. **11**, 229 (1968).
30. S. B. Kormer, M. V. Sinitsyn, and A. I. Kuryapin, Sov. Phys.-JETP **28**, 852 (1969); Ya. B. Zel'dovich, S. B. Kormer, and V. D. Urlin, Sov. Phys.-JETP **28**, 855 (1969).